Optical Beam Steerable Orthogonal Frequency Division Multiplexing (OFDM) Non-Orthogonal Multiple Access (NOMA) Visible Light Communication Using Spatial-Light Modulator Based Reconfigurable Intelligent Surface

Yin-He Jian, Chih-Chun Wang, Chi-Wai Chow [ID], *Senior Member, IEEE*, Wahyu Hendra Gunawan [ID], Tzu-Chieh Wei [ID], Yang Liu [ID], and Chien-Hung Yeh [ID]

Abstract—We put forward and demonstrate a steerable optical beam visible light communication (VLC) system combining orthogonal frequency division multiplexing (OFDM) and non-orthogonal multiple access (NOMA) schemes, and utilizing a spatial light modulator (SLM)-based reconfigurable intelligent surface (RIS) for beam steering. When utilizing the SLM as RIS for optical beam steering, its operation principle, maximum achievable steering angle (i.e., field-of-view, FOV), as well as the corresponding loss should be analyzed. We theoretically and experimentally analyzed in detail the characters of SLM when acting as the RIS. Experimental results demonstrate the flexibility of both active beam control and data rate allocation for multiple users. The SLM-based RIS can independently and simultaneously control multiple beams, and significantly reduce the deploying cost of the increase in the devices for the multi-beam handling scenario. All of the specified channels under evaluation satisfy the pre-forward error correction bit-error rate limit (pre-FEC BER $= 3.8 \times 10^{-3}$).

Index Terms—Free-space optical communication (FSO), non-orthogonal multiple access (NOMA), optical wireless communication (OWC), orthogonal frequency division multiplexing (OFDM), visible light communication (VLC).

I. INTRODUCTION

OPTICAL wireless communication (OWC) is one of the promising technologies for the high-speed requirements

Yin-He Jian, Chih-Chun Wang, Chi-Wai Chow, Wahyu Hendra Gunawan, and Tzu-Chieh Wei are with the Department of Photonics & Graduate Institute of Electro-Optical Engineering, College of Electrical and Computer Engineering, National Yang Ming Chiao Tung University, Hsinchu 30010, Taiwan, and also with the National Chiao Tung University, Hsinchu 30010, Taiwan (e-mail: cwchow@nycu.edu.tw).

Yang Liu is with the Philips Electronics Ltd., Shatin, Hong Kong.

Chien-Hung Yeh is with the Department of Photonics, Feng Chia University, Taichung 40724, Taiwan (e-mail: yehch@fcu.edu.tw).

in the next-generation wireless systems [1], [2], [3]. It can provide abundant bandwidth resource for relaxing the highly congested radio-frequency (RF) communication spectrum [4], [5]. Besides, the immunity of electromagnetic interference (EMI), low-cost deployment and high privacy are also benefited from the utilization of OWC systems. Among these OWC technologies, one realization is the visible light communication (VLC) [6], [7], which can provide both the data transmission and light illumination at the same time [8], [9], [10]. Many VLC systems with the capability of high data rate transmissions have been reported [11], [12], [13], [14], [15], [16], [17]. VLC systems also show their unique and high-performance applications in underwater communication [18], [19] and visible light positioning (VLP) [20], [21], [22]. Hence, VLC is considered as an important candidate for the future 6G networks [23].

The VLC systems can be mainly characterized into two types: the non-line-of-sight (NLOS) diffused systems; and the direct line-of-sight (LOS) systems [24]. They have their own advantages and shortcomings. For example, although the diffused systems can support the NLOS transmission, which is especially useful for the environment with obstacles, the performance is subjected to poor power efficiency, pulse spreading issue and multipath-induced inter-symbol interference (ISI). On the other hand, in spite of preserving from the high received power, the LOS systems require additional mechanisms to ensure that the transmitter (Tx) and receiver (Rx) are precisely faced to each other; and it will become more challenging for catering mobile terminal users. Therefore, several approaches of actively controlling optical beams such as using micro-electro-mechanical system (MEMS) [25], optical phased array (OPA) [26], [27], diffractive optical device [28], tunable liquid lens as well as liquid crystal on silicon (LCoS) based spatial light modulator (SLM) [29] have been proposed recently. In particular, SLM can act as reconfigurable intelligent surface (RIS) [30] in the optical domain and play the role of optical beam steering. RIS

is composed of an array of reflective elements electronically controlled by phase shifters. The RIS have shown its dramatic improvement over system performances via handling with the power-induced low data rate and the sparse channel-induced low rank issues in the RF spectrum. SLM could also be a promising candidate for enhancing the received power through providing the active beam control and beam focusing. Among other optical beam steering techniques, only SLM can independently and simultaneously control multiple beams, significantly reducing the deploying cost of the increase in the devices for the multi-beam handling scenario. Moreover, SLM can be more attractive owing to its compact size, lightweight and low power consumption.

In the future network, it is highly expected to develop point-to-multipoint (PtoM) transmissions in order to accommodate the demands such as Internet of Things (IoT) and mobile user hand-over issue. Though the diffused systems can provide such a link, they are still restricted to aforementioned disadvantages. Non-orthogonal multiple access (NOMA) technique [31], [32], [33] provides an alternative solution and is one of the promising technologies to address these challenges. The features of the NOMA scheme mainly contain the improved spectral efficiency and the massive connectivity [34]. The innovative concept of NOMA schemes can allow multiple users to share the time or the frequency resources via the power or code division multiplexing during the transmission. Specifically, for the power domain multiplexing based NOMA scheme, the basic idea is the combination of the superposition code and the successive interference cancellation (SIC), which will be introduced later. In addition, the NOMA scheme has been proved for being capable of achieving the capacity bound and flexibly allocating different data rate pairs for multiple users.

In this work, we demonstrate an optical beam steerable VLC system combining orthogonal frequency division multiplexing (OFDM) and NOMA schemes, utilizing a SLM-based RIS for beam steering. This work is a follow-up and extended oral presentation in OFC 2023 [32]. Ref. [32] only experimentally demonstrated the feasibility of using SLM for optical beam steering without providing any equations and detail analysis. The key contributions of this work include:

  i) Detail discussion of the successive interference cancellation (SIC) with equations are provided. It allows successful decoding of two or more data that arrive simultaneously.
 ii) Detail characterization of SLM is discussed with equations. Specifically, the relation between the computer-generated holograms (CGHs) and the beam steering efficiency is found.
iii) Analysis of steering loss against the steering angle based on direct simulation and application of derived formula are performed. Compared with the direct simulation, our derivation can provide an intuitive view of connecting CGHs and the steering efficiency.

When utilizing the SLM as RIS for optical beam steering, its operation principle, maximum achievable steering angle (i.e., field-of-view, FOV), as well as the corresponding loss should be analyzed. We theoretically and experimentally analyzed in detail the characters of SLM when acting as the RIS, and a FOV
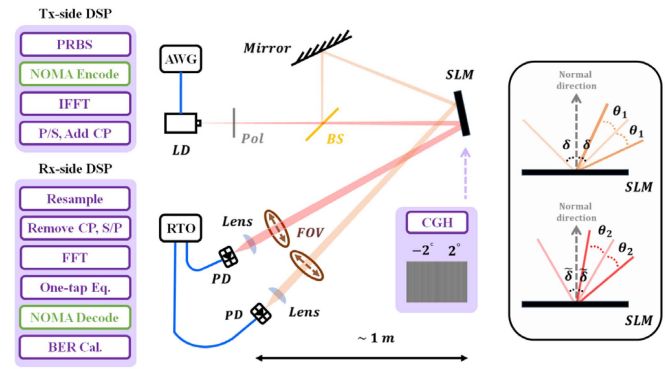

Fig. 1. Experiment of the OFDM-NOMA beam steerable VLC system utilizing the SLM-based RIS. AWG: arbitrary waveform generator; LD: laser diode; BS: beam splitter; Pol: Polarizer; SLM: spatial light modulators; PD: Photodetector; RTO: real-time oscilloscope; CGH: computer generated hologram.

of 4.6° is achieved in the proposed system. The flexibility of both active beam control and data rate allocation for multiple users are demonstrated. By adjusting different power ratios (PRs) in the NOMA scheme, the data rates for user-1 and user-2 of (1.943 Gbit/s, 2.795 Gbit/s) and (2.131 Gbit/s, 1.943 Gbit/s) can be attained when the steering angle is 0° and PR equals to 2.5 and 4, respectively. Moreover, for these two PR values of 2.5 and 4, the data rates for user-1 and user-2 of (1.028 Gbit/s, 1.92 Gbit/s) and (1.903 Gbit/s, 1.267 Gbit/s) with the steering angle of 2° can be obtained. All of the channel pairs can simultaneously satisfy the pre-forward error correction bit error rate (pre-FEC BER = 3.8×10^{-3}) requirement. It is worth to mention that in this proof-of-concept demonstration, only two simultaneous users are supported, the SLM-based RIS could independently and simultaneously control multiple beams, and significantly reduce the deploying cost of the increase in the devices for the multi-beam handling scenario.

II. EXPERIMENTAL SETUP AND NOMA ALGORITHM

Fig. 1 shows the proposed the OFDM-NOMA beam steerable VLC system utilizing the SLM-based RIS for beam steering and focusing. Two independent data sequences are digitally generated and combined using the NOMA algorithm. The detailed process of the NOMA algorithm will be introduced in the next paragraph. After the NOMA encoding, the OFDM encoding is executed, which involves Inverse Fast Fourier Transform (IFFT), parallel-to-serial (P/S) and the addition of the cyclic prefix (CP). The OFDM data sequence is converted to the analog signal via an arbitrary waveform generator (AWG, Tektronix AWG 70001). The optical signal is obtained through driving the analog signal to the laser diode (LD, Thorlabs PL520) with wavelength of 520 nm in this experiment. It is necessary to place one polarizer behind the output of the LD to match the alignment angle of the SLM. In order to simultaneously support the data transmission for two users, the optical beam is divided into two paths via a beam splitter (BS). The measured splitting ratio is 64:36 and the beam with less power is reflected by the mirror with 0.64 dB loss. These two beams are separately adjusted to incident on the different locations of the SLM and the SLM can reflect
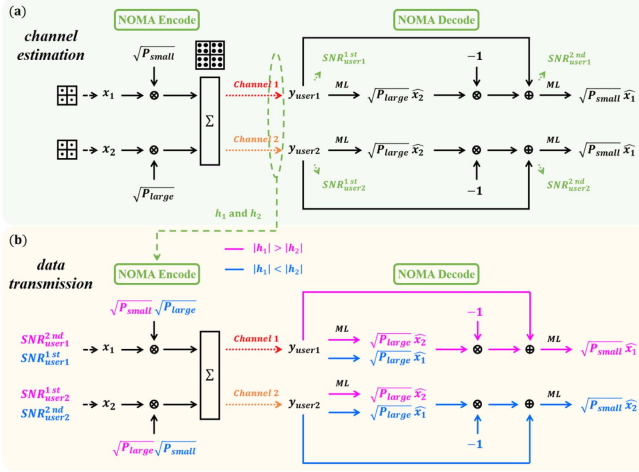
Fig. 2. Flow diagrams of the NOMA algorithm in (a) channel estimation phase and (b) data transmission phase.

the beams in a controlled manner. The operation principle and the performance analysis will be discussed in Section III. The FOV of $\sim 4.6^{\circ}$ provided by the SLM can be achieved. Though the SLM works, in principle, as incident beam is normal, it is allowed to make the incident beam oblique within a small range relative to the normal direction without the performance degradation (i.e., δ and $\tilde{\delta}$ in the rightmost inset of Fig. 1) and it can significantly facilitate the arrangement of the experiment. Therefore, the steering angle (i.e., θ_i for user-i) is defined as the deviation from the reflected beam. Two steering angle pairs (θ_1, θ_2) = (0°, 0°) and (2°, -2°) are tested in this experiment. The optical beam steering is controlled by uploading different CGHs to the SLM-based RIS. It is worth to mention that although only two steering angle pairs are demonstrated, it should be achievable to independently control all of the steering angles within the FOV for two users to support realistic user-moving cases.

The two photodiodes (PD, EOT ET-2030A) with the same specification are located ~ 1 m away from the SLM. The beam sizes for both users are ~ 2 mm. Prior to the reception, the lenses are placed in front of the PDs for focusing. The PDs are attached to a real-time oscilloscope (RTO, Teledyne LeCroy 816ZI-B) and the two signals can be simultaneously captured. The decoding process follows the OFDM decoding, which involves signal resampling, the removal of CP, serial-to-parallel (S/P), Fast Fourier Transform (FFT), one-tap equalization. It is followed by the NOMA decoding to separate two data sequences from each other. Last, the BER is calculated to evaluate the VLC system performance.

The underpinning working principle of the NOMA scheme is the utilization of the superposition code and the SIC. The superposition code permits the summation of data sequences with different powers while the SIC process allows the subtraction over data sequences and makes the decoding iterative. Fig. 2(a) and (b) shows the flow diagrams of the NOMA algorithm, including optic channel estimation phase and data transmission phase. Here, the OFDM encoding and decoding processes are

purposely omitted to simplify the figure. One necessary information that can determine the performance of the NOMA scheme is the decoding order. Therefore, the channel estimation should be performed to acquire the full channel state information (CSI) as shown in Fig. 2(a). In this stage, two independent normalized power 4-quadrature amplitude modulation (QAM) data sequences are scaled with different power and then added up. Without loss of generality, the power used for the data-2 is assumed to be larger (i.e., $\sqrt{P_{\text{large}}}$) than that of the data-1 (i.e., $\sqrt{P_{\text{small}}}$). At the Rx side, the channel coefficients for user-1 and user-2 (i.e., h_1 and h_2) will be estimated. Moreover, in order to further improve the data rates, the signal-to-noise ratio (SNR) distributions are also estimated through the calculation of the average Euclidean Distance between the Tx and Rx data. There are four SNR distributions to be acquired since both users experiences two decoding processes and the SNR distributions can be obtained for each decoding (i.e., SNR_{user1}^{1st}, SNR_{user1}^{2nd}, SNR_{user2}^{1st} and SNR_{user2}^{2nd}). During the decoding process, the first step is to consider the data-2 received by both user-1 and user-2 since data-2 is encoded with larger power. Here, the data-1 is regarded as the noise and the maximum likelihood (ML) detection is employed. The procedure can be expressed as (1) and (2).

$$\sqrt{P_{\text{large}}}\widehat{x}_{2,user1}(i)$$
$$= \arg \max_{m=\{1,2,3,4\}} f\left(y_{user1}(i)|\sqrt{P_{\text{large}}}x_{2,m}\right) \qquad (1)$$

$$\sqrt{P_{\text{large}}}\widehat{x}_{2,user2}(i)$$
$$= \arg \max_{m=\{1,2,3,4\}} f\left(y_{user2}(i)|\sqrt{P_{\text{large}}}x_{2,m}\right) \qquad (2)$$

where $y_{user1}(i)$ and $y_{user2}(i)$ are the i-th received signals after one-tap equalization for user-1 and user-2, respectively. $\{\sqrt{P_{\text{large}}}x_{2,m}|m=1,2,3,4\}$ stands for the set of normalized 4-QAM scaled with $\sqrt{P_{\text{large}}}$. $\widehat{x}_{2,user1}(i)$ and $\widehat{x}_{2,user2}(i)$ are the i-th estimated symbols of the data-2 for user-1 and user-2, respectively. $f(x)$ stands for the Gaussian probability density function (PDF). The SNR distributions for the first decoding (i.e., SNR_{user1}^{1st} and SNR_{user2}^{1st}) are estimated using (3) and (4).

$$SNR_{user1}^{1st} = \frac{1}{N}\sum_i \frac{|\sqrt{P_{\text{large}}}x_2(i)|^2}{|y_{user1}(i) - \sqrt{P_{\text{large}}}x_2(i)|^2} \qquad (3)$$

$$SNR_{user2}^{1st} = \frac{1}{N}\sum_i \frac{|\sqrt{P_{\text{large}}}x_2(i)|^2}{|y_{user2}(i) - \sqrt{P_{\text{large}}}x_2(i)|^2} \qquad (4)$$

where $\sqrt{P_{\text{large}}}x_2(i)$ is i-th symbol of the data-2 scaled with $\sqrt{P_{\text{large}}}$ and N is the data length of the data-2. Then, with the estimated data-2, the SIC is performed to obtain the data-1, which means that the estimated data-2 sequence will be subtracted from the received signals for both user-1 and user-2. It can be mathematically written as (5) and (6).

$$\sqrt{P_{\text{small}}}\widehat{x}_{1,user1}(i)$$
$$= \arg \max_{m=\{1,2,3,4\}}$$

$$f\left(\left(y_{user1}(i) - \sqrt{P_{large}}\widehat{x}_{2,user1}(i)\right)\Big|\sqrt{P_{small}}x_{1,m}\right) \quad (5)$$

$$\sqrt{P_{small}}\widehat{x}_{1,user2}(i)$$

$$= \arg\max_{m=\{1,2,3,4\}}$$

$$f\left(\left(y_{user2}(i) - \sqrt{P_{large}}\widehat{x}_{2,user2}(i)\right)\Big|\sqrt{P_{small}}x_{1,m}\right) \quad (6)$$

where $\{\sqrt{P_{small}}x_{1,m}|m=1,2,3,4\}$ stands for the set of normalized 4-QAM scaled with $\sqrt{P_{small}}$, $\widehat{x}_{1,user1}(i)$ and $\widehat{x}_{1,user2}(i)$ are the i-th estimated symbols of the data-1 for user-1 and user-2. The SNR distributions for the second decoding (i.e., SNR_{user1}^{2nd} and SNR_{user2}^{2nd}) are estimated using (7) and (8).

$$SNR_{user1}^{2nd}$$
$$= \frac{1}{N}\sum_i \frac{|\sqrt{P_{small}}x_1(i)|^2}{|y_{user1}(i) - \sqrt{P_{large}}\widehat{x}_{2,user1}(i) - \sqrt{P_{small}}x_1(i)|^2} \quad (7)$$

$$SNR_{user2}^{2nd}$$
$$= \frac{1}{N}\sum_i \frac{|\sqrt{P_{small}}x_1(i)|^2}{|y_{user2}(i) - \sqrt{P_{large}}\widehat{x}_{2,user2}(i) - \sqrt{P_{small}}x_1(i)|^2} \quad (8)$$

where $\sqrt{P_{small}}x_1(i)$ is i-th symbol of the data-1 scaled with $\sqrt{P_{small}}$.

In the stage of data transmission, the power ratio (PR, i.e., $\sqrt{P_{large}/P_{small}}$), which has been specified in the channel estimation remains unchanged. The absolute value of h_1 and h_2 are compared with each other to determine the decoding order, as shown in Fig. 2(b). The principle of arranging the decoding order is that the poorer channel (i.e., smaller $|h|$) will be decoded, in general, with less SIC iterations. This means the corresponding data sequence for this channel should be encoded with the larger power (i.e., $\sqrt{P_{large}}$) and there is no need to decode twice for this data sequence. Besides, the bit-loading is also applied based on SNR distributions acquired from the channel estimation phase. The purple lines shown in Fig. 2(b) illustrate the NOMA encoding and decoding processes in the case of the better channel of user-1 (i.e., $|h_1|>|h_2|$). In the encoding part, bit-loaded data sequences of the data-1 and the data-2 according to SNR_{user1}^{2nd} and SNR_{user2}^{1st} distributions are generated and encoded with $\sqrt{P_{small}}$ and $\sqrt{P_{large}}$, respectively. In the decoding part, (9)–(11) will be applied to obtain these two data sequences.

$$\sqrt{P_{large}}\widehat{x}_{2,user1}(i) = \arg\max_m f\left(y_{user1}(i)|\sqrt{P_{large}}x_{2,m}\right) \quad (9)$$

$$\sqrt{P_{small}}\widehat{x}_{1,user1}(i) = \arg\max_m f\left((y_{user1}(i) - \sqrt{P_{large}}\widehat{x}_{2,user1}(i))\Big|\sqrt{P_{small}}x_{1,m}\right) \quad (10)$$

$$\sqrt{P_{large}}\widehat{x}_{2,user2}(i) = \arg\max_m f\left(y_{user2}(i)|\sqrt{P_{large}}x_{2,m}\right) \quad (11)$$
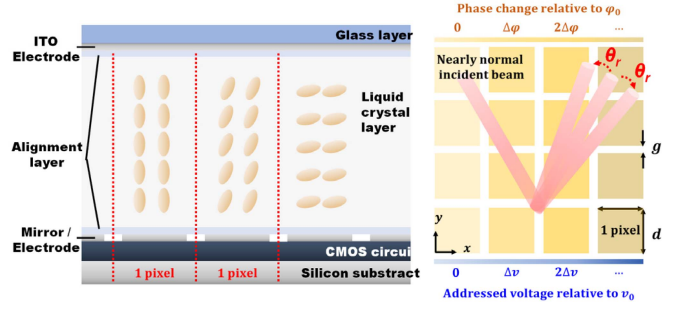

Fig. 3. Schematic diagram of the working principle of the SLMs.

where the cardinalities of the sets $\{x_{1,m}\}$ and $\{x_{2,m}\}$ depend on the SNR_{user1}^{2nd} and SNR_{user2}^{1st} distributions. Similarly, the NOMA encoding and decoding processes for the case of the better channel of user-2 (i.e., $|h_1|<|h_2|$) are illustrated as the blue lines shown in Fig. 2(b). In accordance with SNR_{user1}^{1st} and SNR_{user2}^{2nd} distributions, the data-1 and the data-2 are encoded with $\sqrt{P_{large}}$ and $\sqrt{P_{small}}$, respectively. Thereby, (12)–(14) will be performed during the decoding.

$$\sqrt{P_{large}}\widehat{x}_{1,user1}(i) = \arg\max_m f\left(y_{user1}(i)|\sqrt{P_{large}}x_{1,m}\right) \quad (12)$$

$$\sqrt{P_{large}}\widehat{x}_{1,user2}(i) = \arg\max_m f\left(y_{user2}(i)|\sqrt{P_{large}}x_{1,m}\right) \quad (13)$$

$$\sqrt{P_{small}}\widehat{x}_{2,user2}(i) = \arg\max_m f\left((y_{user2}(i) - \sqrt{P_{large}}\widehat{x}_{1,user2}(i))\Big|\sqrt{P_{small}}x_{2,m}\right) \quad (14)$$

One great advantage of the NOMA scheme is the flexibility of the data rate allocation for multi-users, which is achieved by adjusting the PR for different users. In this proof-of-concept experiment, two PR values are chosen, including PR of 2.5 and 4.0, and different data rate pairs are demonstrated.

III. OPERATION PRINCIPLE OF SLMS AND PERFORMANCE ANALYSIS

When utilizing the SLM as RIS for optical beam steering, its operation principle, maximum achievable steering angle, as well as the corresponding loss should be analyzed. The SLMs act as optical 2-dimensional (2D) phase arrays to provide the active control of optical beams. The SLM consists of a liquid crystal (LC), a reflective and two electrode layers. One electrode is based on transparent indium tin oxide (ITO) material allowing light to pass through. The LC layer can be controlled by pixel electrodes, at which different addressed grayscale voltages can tilt the angle of the LC axes to provide different phase changes. There are many applications through providing phase changes for each pixel, such as the beam steering, holograms, and the generation of orbital angular momentum (OAM) beams, etc.

Fig. 3 illustrates the schematic diagram of the working principle of the SLM for beam steering. The voltages applied to pixel

electrodes are addressed at a fixed voltage spacing Δv; hence, the corresponding phase changes at a fixed spacing $\Delta\varphi$ will be produced accordingly. Provided that one addressed voltage corresponds to one grayscale value, all addressed voltages will produce one CGH pattern, and it will be uploaded to the SLM. Let the aperture size and the gap between two adjacent pixels are d and g, respectively. The pitch and filling factor of the SLM can be defined as $D = d + g$ and $r = d/D$, respectively. Owing to the artificially generated grating structure pattern (i.e., CGH pattern) inside the SLM, the component of wave vector can be adjusted depending on the phase change $\Delta\varphi$ per pixel provided by the SLM. The relation can be written as (15), where θ_i and θ_r are the incident and the reflected angles of the beam, respectively.

$$\frac{2\pi}{\lambda}\left(\sin\theta_r - \sin\theta_i\right)D = \Delta\varphi \tag{15}$$

Assume that the incident beam is normal to the SLM, the steering angle of the 0-order spot given the phase spacing $\Delta\varphi$ can be calculated by (16) and the FOV can be expressed in (17) by substituting the maximum phase change per pixel with π rad.

$$\theta_r = \sin^{-1}\left(\frac{\lambda\Delta\varphi}{2\pi D}\right) \tag{16}$$

$$FOV = 2\sin^{-1}\left(\frac{\lambda}{2D}\right) \tag{17}$$

It is worth to note that the FOV of the SLM depends on the working wavelength λ and the pitch D. As illustrated in (17), larger FOV can be achieved if we extend the wavelength to a longer wavelength band (e.g., from the visible light to C-band). Moreover, when the pitch D decreases, larger FOV can also be obtained. However, decreasing D will lead to more pixel crosstalk, resulting in the accuracy degradation for the phase control.

The SLM used for the experiment has a pitch D of 6.4 μm, filling factor r of 0.93 and the working wavelength of 520 nm and the quantized voltage of 8-bit resolution (i.e., 256 grayscale levels). The FOV is calculated to be 4.6°. The simulation is implemented via Matlab. In this simulation, Fraunhofer diffraction is assumed and the object plane is set at the output of the SLM. Moreover, the edge effect is neglected since the beam size is much smaller than the panel size of the SLM. Also, the intrinsic SLM loss such as absorption is not considered. Provided that the input is the plane wave, the phase change supported by the CGH with the exact dimension (e.g., the pitch d and the gap g of the SLM) contains all information required at the object plane and the Fourier transform (FT) can be conducted. The image plane is set to be 1 m away from the SLM and the intensity is normalized to be unity. The simulation result of the beam steering using these parameters at different steering angles is shown in Fig. 4(a). As illustrated in Fig. 4(a), the FOV represents the maximum achievable steering angle of the 0-order light beam. However, when the steering angle is larger than the FOV, the 0-order light spot will be significantly attenuated, and the corresponding 1-order light spot will appear within the FOV range as also illustrated in Fig. 4(a). As shown in Fig. 4(a), the position difference (i.e., x-axis) between the 0-order and 1-order
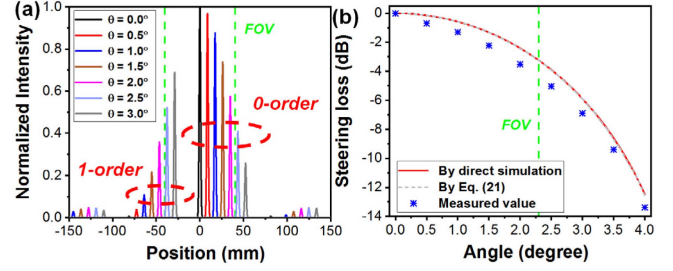

Fig. 4. Simulation results of (a) the steered optical signals at different steering angles and positions at the image plane 1 m away; (b) the steering losses at different steering angles.

beams for a particular angle is fixed. When the steering angle of the 0-order beam is larger than the FOV, the optical intensity will drop significantly similar to the optical phase array effect described in [27], and the 1-order beam will move inside the FOV range. Due to the conservation of energy, the intensity of the 1-order beam will increase accordingly

Apart from the direct simulation, the steering losses against the different steering angles are also mathematically characterized. The behavior of the derivation of the optical beam can be well-modeled from the perspective of the Fraunhofer diffraction in Fourier optics. As illustrated in Fig. 3, for a given fixed pitch D, the periodic voltages applied to different pixel-columns in the SLM via the uploaded CGH file will produce the periodic phase shift pattern correspondingly. This periodic phase shift pattern forms the optical grating structure needed for optical beam steering. The optical grating structure in the SLM is similar to the optical phase array described in [27]. When the optical steering angle is large, the optical intensity will drop accordingly. To be specific, we define two positive integers n and m, where n as the smallest number such that $256 \times n$ can be divisible by a positive number m. Note that the grayscale value of 256 corresponds to the phase change of 2π. Following this definition, the phase change of $n / m \times 2\pi$ per pixel results in periodic structure of mD. For example, if the grayscale values follow the set {0, 85, 170}, the corresponding (m, n) is (3, 1) and if the grayscale values follow the set {0, 102, 204, 51, 153}, where the gray-scale values of 51 and 153 are equivalent to those of 306 and 408, the corresponding (m, n) is (5, 2). The phase function supported by the SLM, as the mathematical expression along the x-axis in Fig. 3(b), can be written as (18).

$$p(x) = e^{j2\pi\frac{n}{m}\left\lceil\frac{x}{D}\right\rceil}$$
$$\times l\left(i < \frac{x}{D} < i + r, i \in \{0, 1, \ldots, m-1\}\right) \tag{18}$$

where r is the filling factor, x is the position variable at the objective plane, n as the smallest number such that $256 \times n$ can be divisible by a positive number m. l is the indicator function, where l(true) and l(false) will return one and zero, respectively. Since $p(x)$ is periodic over mD, the corresponding Fourier Transform is a series of delta functions scaled with $2\pi a_k$ standing at the frequencies of $\omega_k = 2\pi k/mD$. The coefficients a_k can be

calculated as (19) and further simplified and rearranged in (20).

$$a_k = \frac{1}{-jk2\pi}\left(e^{-jkr\frac{2\pi}{m}} - 1\right)e^{j2\pi\frac{n}{m}}\frac{1 - e^{-j2\pi(n-k)}}{1 - e^{-j2\pi/m(n-k)}} \tag{19}$$

$$a_{n+qm} = \frac{m}{-j(n+qm)2\pi}\left(e^{-j(n+qm)r\frac{2\pi}{m}} - 1\right)e^{j2\pi\frac{n}{m}} \tag{20}$$

where $k = n + qm$ for those integer q. The other a_k turn out to be zeros. From the Fraunhofer diffraction theory, the axis of frequency domain of the object plane can be connected to that of the space domain of the image plane. By the correspondence of two axes, the location of the 0-order beam can be shown to be located at $k = n$ (i.e., $q = 0$). It is noted that one CGH and one corresponding steering angle has the specified and unique (m, n) pair. Therefore, the intensity of the 0-order beam can be obtained by means of substituting (m, n) into (20), setting $q = 0$ and taking its norm. By the proper normalization, the steering loss induced by the LC periodic structure for 0-order beam can be simplified as a compact form and shown in (21).

$$|a_n|^2 = \left(\frac{m}{\pi n}\right)^2 \sin^2\left(r\frac{\pi n}{m}\right) \tag{21}$$

Fig. 4(b) shows the simulated steering loss against the steering angle obtained from the direct simulation and the application of (21), as well as the measured loss. We can observe the three results are match with each other. The power meter (Thorlabs PM100D and S120C) has the diameter of 9.5 mm, which is large enough to receive the beam spot. The power in the simulation and the measurement are respectively normalized by those of at the steering angle of 0^0 (i.e., $\lim_{m\to\infty}\sup|a_n|^2$ for (21)). It should be noted that in the experiment, there exists the reflection at the steering angle of $0°$ from the external glass, accounting for roughly 2.97% of the total power. Hence, only 97.03% of measured power is actually interacted with the LC so that it should be controllable (and thereby steerable). From Fig. 4(b), it is observed slight differences between the theoretical values and the measured values. First, at the steering angle of 0^0, the measured value is higher than the theoretical one by 0.13 dB. This could be explained from the additional reflection of the glass as mentioned. For other measured values, they are below the theoretical ones. Specifically, the differences are 0.43 dB, 0.58 dB, 0.77 dB and 0.94 dB for the steering angles of 0.5^0, 1.0^0, 1.5^0 and 2.0^0. These differences could be attributed to the intrinsic loss induced by the LC, the non-uniform electric field applied to the LC and the non-linear voltage-phase relationship of the SLM used for the experiment. Further calibration of the SLM allows the mitigation of the latter two non-ideal effects and can improve the steering loss.

IV. RESULTS AND DISCUSSION

The proof-of-concept experimental demonstration of the proposed OFDM-NOMA beam steerable VLC system utilizing SLM-based RIS as depicted in Fig. 1 is performed. Here, we illustrate the feasibility and flexibility of optical beam steering and data rate assignment to two users. For the former, two steering angle pairs $(\theta_1, \theta_2) = (0°, 0°)$ and $(2°, -2°)$ are used;
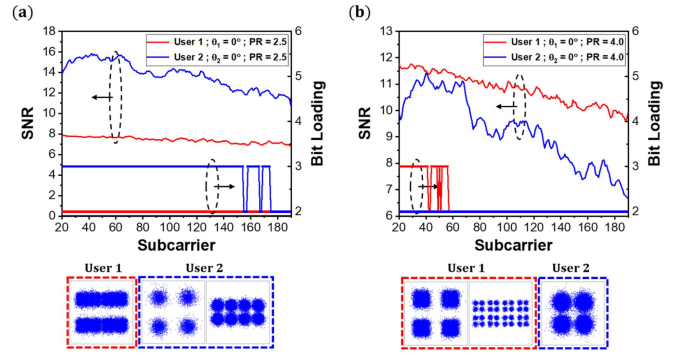

Fig. 5. SNR distributions, the corresponding bit loadings and their realizations for user-1 and user-2 at the $(\theta_1, \theta_2) = (0°, 0°)$ over different power ratios (a) PR = 2.5 and (b) PR = 4.0.

and for the latter, two power ratios PR = 2.5 and 4.0 in the NOMA scheme are also evaluated.

The optical power after the polarizer is fixed at 7.27 dBm. The optical powers of 0.86 dBm and 3.77 dBm are measured at user-1 and user-2 positions as the steering angle is $(\theta_1, \theta_2) = (0°, 0°)$. However, the powers of only -3.28 dB and -0.09 dBm are obtained for user-1 and user-2 as the steering angle increases to $(\theta_1, \theta_2) = (2°, -2°)$. The reason for the reduction of the power has been discussed in Section III above. It turns out that for the NOMA scheme, user-2 experiences the better channel so that SIC should be performed while the poor channel of user-1 implies only one decoding process. Therefore, the data sequences for user-1 and user-2 should be encoded with $\sqrt{P_{large}}$ and $\sqrt{P_{small}}$, respectively; and during the decoding process, (12)–(14) will be applied.

Fig. 5(a) and (b) show the measured SNR distributions, the corresponding bit loadings and their realizations of the constellations for user-1 and user-2 at the PR of 2.5 and 4.0, respectively when the steering angle is $(\theta_1, \theta_2) = (0°, 0°)$. The red lines represent for user-1 and the blue ones is for user-2. The data rates achieved in Fig. 5(a) (i.e., PR = 2.5) are 1.943 Gbit/s for user-1 and 2.795 Gbit/s for user-2. Besides, the data rates achieved in Fig. 5(b) (i.e., PR = 4.0) are 2.131 Gbit/s for user-1 and 1.943 Gbit/s for user-2. The realizations of the constellations shown in Fig. 5(a) and (b) clearly illustrate the received signals for user-1 and user-2. In the constellation of user-1 at PR = 2.5, "small" 8-QAM data around the origin 4-QAM data is observed, and similarly at PR = 4.0, "small" 4-QAM data around the origin 4-QAM and 8-QAM is observed. This is owing to only one decoding process applied to user-1, in which the data of user-2 is regarded as the noise. However, the constellations of user-2 at both PR = 2.5 and PR = 4.0 look normal as the typical QAM data due to the implementation of the SIC. Moreover, if we look into the SNR distributions of user-1 from PR = 2.5 to PR = 4.0, the rise of $\sim$ 3 dB can be seen, which is because the user-1 is encoded with $\sqrt{P_{large}}$ so that the rise of PR implies the increase of the $\sqrt{P_{large}}$. The drop of SNR distributions of user-2 can be interpreted in the similar fashion.

Fig. 6(a) and (b) show the measured SNR distributions, the corresponding bit loadings and their realizations of the constellations for user-1 and user-2 at the PR of 2.5 and 4.0, respectively,
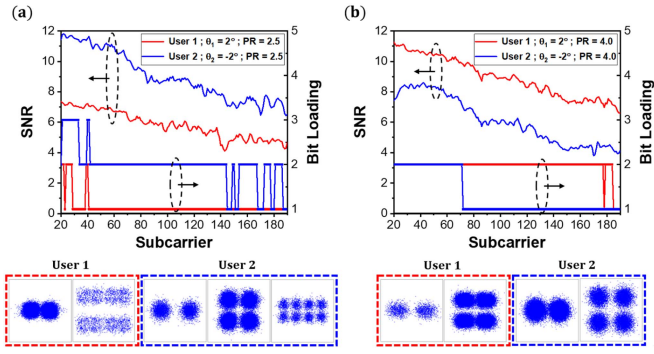
Fig. 6. SNR distributions, the corresponding bit loadings and their realizations for user-1 and user-2 at the $(\theta_1, \theta_2) = (2^o, -2^o)$ over different power ratios (a) PR = 2.5 and (b) PR = 4.0.
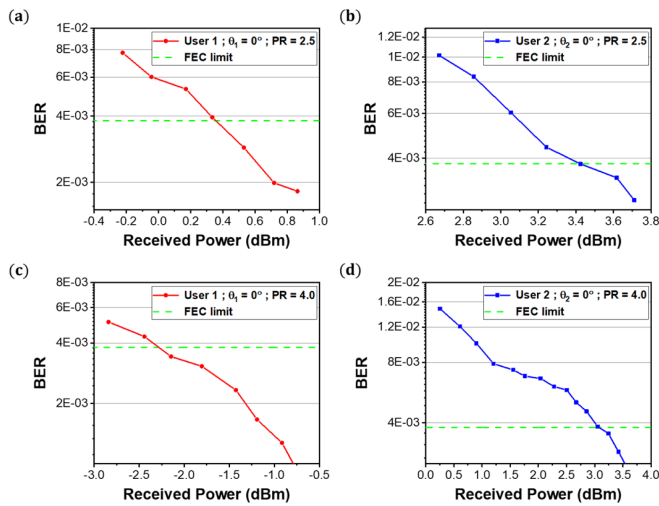

Fig. 7. BERs against received powers of (a) User-1 at $\theta_1 = 0^o$ and PR = 2.5, (b) User-2 at $\theta_2 = 0^o$ and PR = 2.5, (c) User-1 at $\theta_1 = 0^o$ and PR = 4.0 and (d) User-2 at $\theta_2 = 0^o$ and PR = 4.0.

Fig. 8. BERs against received powers of (a) User-1 at $\theta_1 = 2^o$ and PR = 2.5, (b) User-2 at $\theta_2 = -2^o$ and PR = 2.5, (c) User-1 at $\theta_1 = 2^o$ and PR = 4.0 and (d) User-2 at $\theta_2 = -2^o$ and PR = 4.0.

when the steering angle is $(\theta_1, \theta_2) = (2^o, -2^o)$. The data rates achieved in Fig. 6(a) (i.e., PR = 2.5) are 1.028 Gbit/s for user-1 and 1.92 Gbit/s for user-2. Also, the data rates achieved in Fig. 6(b) (i.e., PR = 4.0) are 1.903 Gbit/s for user-1 and 1.267 Gbit/s for user-2. The realizations of the constellations and the rise/drop of the SNR distributions of user-1/user-2 can be explained in the same manner as Fig. 5(a) and (b).

The BER measurements of the proposed OFDM-NOMA beam steerable VLC system utilizing SLM-based RIS are performed and shown in Fig. 7(a)–(d). and 8(a)–(d) at different steering angles respectively. With the previously specified data rates and the steering angle of 0°, Fig. 7(a)–(d) show the BERs of user-1 at the PR of 2.5, user-2 at the PR of 2.5, user-1 at the PR of 4.0 and user-2 at the PR of 4.0, respectively; and similarly, with the previously specified data rates and the steering angle of 2° and -2°, Fig. 8(a)–(d) show the BERs of user-1 at the PR of 2.5, user-2 at the PR of 2.5, user-1 at the PR of 4.0 and user-2 at the PR of 4.0, respectively. The results indicate that all of the data rate pairs can be simultaneously satisfied the pre-FEC BER (i.e., 3.8×10^{-3}). In the experiment, the Rxs is re-aligned
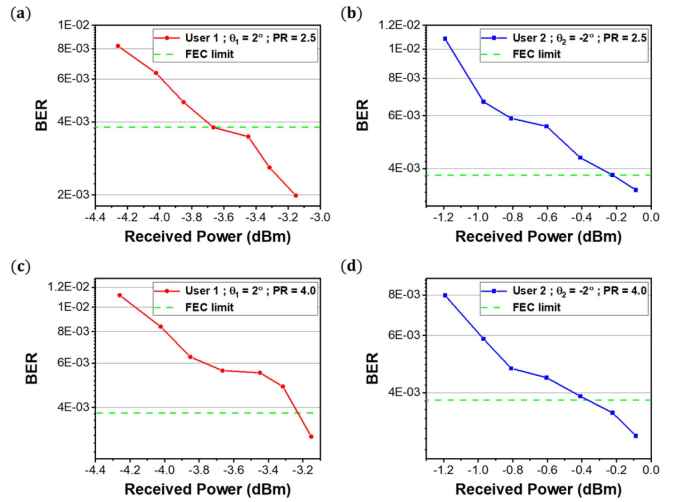
after the optical beam steering to retrieve the highest possible performance. The coverage area for both users in this proposed system at 1 m away from the SLM is 8 cm × 8 cm [i.e., 8 cm = 1 m × tan(4.6°)]. According to the FOV analysis discussed in (17), using infrared (IR) wavelengths or using an SLM with smaller pitches can increase the coverage area. In addition, an angle magnifier can be introduced at the output of the SLM to further increase the FOV [35].

V. CONCLUSION

The ability of active beam control as well as the capability of supporting multiple user transmission scenario becomes more and more crucial in the modern OWC systems. In this work, we demonstrated an optical beam steerable VLC system combined OFDM and NOMA schemes, utilizing the SLM-based RIS for beam steering. In this proof-of-concept demonstration, only two simultaneous users were supported, the SLM-based RIS could independently and simultaneously control multiple beams. Hence, the adoption of the SLM can reduce the deploying cost of the increase in the devices for the multi-beam handling scenario. We also theoretically and experimentally analyzed in detail the characters of SLM when acting as the RIS, and a FOV of 4.6° was achieved in the proposed system. Though the demonstrated FOV is limited, it can be relaxed by extending the wavelength to the longer band. The flexibility of both active beam control and data rate allocation are demonstrated, showing the data rates for user-1 and user-2 of (1.943 Gbit/s, 2.795 Gbit/s) and (2.131 Gbit/s, 1.943 Gbit/s) can be attained when the steering angle is 0°; and the data rates for user-1 and user-2 of (1.028 Gbit/s, 1.92 Gbit/s) and (1.903 Gbit/s, 1.267 Gbit/s) with the steering angle of 2° can be also reached. All of the data rate pairs can simultaneously fulfill the pre-FEC BER (i.e., 3.8×10^{-3}) requirement.

References

[1] K. Wang et al., "Evolution of short-range optical wireless communications," in *Proc. Opt. Fiber Commun. Conf. Exhib.*, 2022, Paper Tu3C.4.

[2] T. Koonen, J. Oh, K. Mekonnen, Z. Cao, and E. Tangdiongga, "Ultra-high capacity indoor optical wireless communication using 2D-steered pencil beams," *J. Lightw. Technol.*, vol. 34, no. 20, pp. 4802–4809, Oct. 2016.

[3] C. W. Chow et al., "Enabling techniques for optical wireless communication systems," in *Proc. Opt. Fiber Commun. Conf. Exhib.*, 2020, Paper M2F.1.

[4] C. Lim and A. Nirmalathas, "Radio-over-fiber technology: Present and future," *J. Lightw. Technol.*, vol. 39, no. 4, pp. 881–888, Feb. 2021.

[5] M. Y. Huang, Y. W. Chen, R. K. Shiu, H. Wang, and G. K. Chang, "A bi-directional multi-band, multi-beam mm-wave beamformer for 5G fiber wireless access networks," *J. Lightw. Technol.*, vol. 39, no. 4, pp. 1116–1124, Feb. 2021.

[6] D. C. O'Brien, L. Zeng, H. Le-Minh, G. Faulkner, J. W. Walewski, and S. Randel, "Visible light communications: Challenges and possibilities," in *Proc. IEEE 19th Int. Symp. Pers., Indoor Mobile Radio Commun.*, 2008, pp. 1–5.

[7] C. W. Chow, C. H. Yeh, Y. Liu, and Y. F. Liu, "Digital signal processing for light emitting diode based visible light communication," *IEEE Photon. Soc. Newslett.*, vol. 26, no. 5, pp. 9–13, Oct. 2012.

[8] T. C. Wu, Y. C. Chi, H. Y. Wang, C. T. Tsai, Y. F. Huang, and G. R. Lin, "Tricolor R/G/B laser diode based eye-safe white lighting communication beyond 8 Gbit/s," *Sci. Rep.*, vol. 7, 2017, Art. no. 11.

[9] C. W. Chow, C. H. Yeh, Y. F. Liu, and Y. Liu, "Improved modulation speed of LED visible light communication system integrated to main electricity network," *Electron. Lett.*, vol. 47, pp. 867–868, 2011.

[10] L. Y. Wei et al., "6.915-Gbit/s white-light phosphor laser diode-based DCO-OFDM visible light communication (VLC) system with functional transmission distance," *Electron. Lett.*, vol. 56, pp. 945–947, 2020.

[11] H. L. Minh et al., "100-Mb/s NRZ visible light communications using a post-equalized white LED," *IEEE Photon. Technol. Lett.*, vol. 21, no. 15, pp. 1063–1065, Aug. 2009.

[12] J. Vučić, C. Kottke, S. Nerreter, K. D. Langer, and J. W. Walewski, "513 Mbit/s visible light communications link based on DMT-modulation of a white LED," *J. Lightw. Technol.*, vol. 28, no. 24, pp. 3512–3518, Dec. 2010.

[13] H. Haas, "Visible light communication," in *Proc. Opt. Fiber Commun. Conf. Exhib.*, 2015, Paper Tu2G.5.

[14] C. Lee et al., "Gigabit-per-second white light-based visible light communication using near-ultraviolet laser diode and red-, green-, and blue-emitting phosphors," *Opt. Exp.*, vol. 25, pp. 17480–17487, 2017.

[15] C. L. Ying, H. H. Lu, C. Y. Li, C. J. Cheng, P. C. Peng, and W. J. Ho, "20-Gbps optical LiFi transport system," *Opt. Lett.*, vol. 40, pp. 3276–3279, 2015.

[16] H. Chun, A. Gomez, C. Quintana, W. Zhang, G. Faulkner, and D. O'Brien, "A wide-area coverage 35 Gb/s visible light communications link for indoor wireless applications," *Sci. Rep.*, vol. 9, 2019, Art.no. 4952.

[17] L. Y. Wei, C. W. Chow, G. H. Chen, Y. Liu, C. H. Yeh, and C. W. Hsu, "Tricolor visible-light laser diodes based visible light communication operated at 40.665 Gbit/s and 2 m free-space transmission," *Opt. Exp.*, vol. 27, pp. 25072–25077, 2019.

[18] C. Shen et al., "20-meter underwater wireless optical communication link with 1.5 Gbps data rate," *Opt. Exp.*, vol. 24, pp. 25502–25509, 2016.

[19] C. Y. Li et al., "An 82-m 9 Gb/s PAM4 FSO-POF-UWOC convergent system," *IEEE Photon. J.*, vol. 11, no. 1, Feb. 2019, Art. no. 7900609.

[20] T. Q. Wang, Y. A. Sekercioglu, A. Neild, and J. Armstrong, "Position accuracy of time-of-arrival based ranging using visible light with application in indoor localization systems," *J. Lightw. Technol.*, vol. 31, no. 20, pp. 3302–3308, Oct. 2013.

[21] L. S. Hsu et al., "Using data pre-processing and convolutional neural network (CNN) to mitigate light deficient regions in visible light positioning (VLP) systems," *J. Lightw. Technol.*, vol. 40, no. 17, pp. 5894–5900, Sep. 2022.

[22] L. Hsu et al., "3-Dimensional visible light positioning (VLP) using two-stage neural network (TSNN) and signal-strength-enhancement (SSE) to mitigate light non-overlapping regions," in *Proc. Eur. Conf. Opt. Commun.*, 2022, Paper Tu5.52.

[23] N. Chi, Y. Zhou, Y. Wei, and F. Hu, "Visible light communication in 6G: Advances, challenges, and prospects," *IEEE Veh. Technol. Mag.*, vol. 15, no. 4, pp. 93–102, Dec. 2020.

[24] L. Grobe et al., "High-speed visible light communication systems," *IEEE Commun. Mag.*, vol. 51, no. 12, pp. 60–66, Dec. 2013.

[25] R. W. Kingsbury, T. Nguyen, K. Riesing, and K. Cahoy, "Fast-steering solutions for cubesat-scale optical communications," *Proc. SPIE*, vol. 10563, 2014, Art. no. 105630G.

[26] P. C. Kuo et al., "Actively steerable integrated optical phased array (OPA) for optical wireless communication (OWC)," in *Proc. Opt. Fiber Commun. Conf.*, 2022. Paper M1C.7.

[27] C. W. Chow et al., "Actively controllable beam steering optical wireless communication (OWC) using integrated optical phased array (OPA)," *J. Lightw. Technol.*, vol. 41, no. 4, pp. 1122–1128, Feb. 2023.

[28] T. Koonen, F. Gomez-Agis, F. Huijskens, K. A. Mekonnen, Z. Cao, and E. Tangdiongga, "High-capacity optical wireless communication using two-dimensional IR beam steering," *J. Lightw. Technol.*, vol. 36, no. 19, pp. 4486–4493, Oct. 2018.

[29] F. Feng, I. H. White, and T. D. Wilkinson, "Free space communications with beam steering a two-electrode tapered laser diode using liquid-crystal SLM," *J. Lightw. Technol.*, vol. 31, no. 12, pp. 2001–2007, Jun. 2013.

[30] A. R. Ndjiongue, T. M. N. Ngatched, O. A. Dobre, and H. Haas, "Reconfigurable intelligent surface-based VLC receivers using tunable liquid-crystals: The concept," *J. Lightw. Technol.*, vol. 39, no. 10, pp. 3193–3200, May 2021.

[31] A. Adnan, Y. Liu, C. W. Chow, and C. H. Yeh, "Demonstration of non-hermitian symmetry (NHS) IFFT/FFT size efficient OFDM non-orthogonal multiple access (NOMA) for visible light communication," *IEEE Photon. J.*, vol. 12, no. 3, Jun. 2020, Art. no. 7201405.

[32] Y. H. Jian et al., "Optical beam steerable and flexible data rate orthogonal frequency division multiplexing non-orthogonal multiple access (OFDM-NOMA) visible light communication," in *Proc. Opt. Fiber Commun. Conf. Exhib.*, 2023, Paper M4F.3.

[33] J. Shi, Y. Hong, R. Deng, J. He, and L. K. Chen, "Real-time software-reconfigurable hybrid in-house access with OFDM-NOMA," *IEEE Photon. Technol. Lett.*, vol. 32, no. 7, pp. 379–382, Apr. 2020.

[34] L. Dai, B. Wang, Y. Yuan, S. Han, I. Chih-lin, and Z. Wang, "Non-orthogonal multiple access for 5G: Solutions, challenges, opportunities, and future research trends," *IEEE Commun. Mag.*, vol. 53, no. 9, pp. 74–81, Sep. 2015.

[35] A. Gomez et al., "Beyond 100-Gb/s indoor wide field-of-view optical wireless communications," *IEEE Photon. Technol. Lett.*, vol. 27, no. 4, pp. 367–370, Feb. 2015.